Transient Model of Preheating a Submerged Entry Nozzle

Y. Li, B.G. Thomas

Department of Mechanical Science and Engineering,
University of Illinois at Urbana-Champaign,
1206 W. Green Street, Urbana, IL, USA, 61801
Phone: (217) 333-6919
Fax: (217) 244-6534
Email: bgthomas@illinois.edu

Keywords: Preheating, nozzle, refractory, combustion, fuel component, torch configuration, flame temperature, contact resistance

ABSTRACT

Adequate preheating of the submerged entry nozzle (SEN) is important to avoid problems such as cracks and skulling, and depends on torch configuration, fuel, SEN geometry and other factors. A steady-state axisymmetric computational model of the flame, combustion reactions, and air entrainment has been combined with a transient model of heat transfer in the refractory walls to simulate the SEN preheating process. The model predictions match with experimental measurements of preheating with a natural-gas torch, including temperature profile across the flame, temperature histories measured inside the SEN wall, the flame shape, and the SEN outer wall temperature distribution. A simple spread-sheet model is introduced to accurately predict flame temperature, heat transfer coefficients and product properties for simple models of SEN preheating, given the air entrainment predicted from the combustion model. The results reveal the times required to reach adequate preheating temperature. Moreover, optimal positioning of the torch above the top of the SEN decreases ambient air entrainment, which increases the temperatures and shortens preheating time.

INTRODUCTION

Torch heating is an important industrial process that is widely used in the steel industry for scarfing, cutting, and preheating of refractories. An important example is the Submerged Entry Nozzle (SEN), which delivers liquid steel from the tundish to the continuous-casting mold, and must be preheated properly to prevent problems such as cracks from thermal shock, and freezing (skulling) of the steel during initial filling. An accurate model simulation of SEN preheating would be useful to optimize this and similar processes, and depends on fuel composition, time needed to reach adequate preheating temperature, and torch configuration.

In torch heating, natural gas is a widely used fuel, often using both air and oxygen as oxygen sources for the combustion. Natural gas is mainly composed of methane, which comprises up to 94% volume fraction. Fundamental burning characteristics of methane with oxygen have been studied by several researchers, both numerically and experimentally. Research into the detailed chemical reaction mechanisms of natural gas ignition and flame has been sponsored by the Gas Research Institute (GRI), creating a comprehensive software database, GRI-Mech. This database includes input files for another software tool, CHEMKIN, which can be used to solve chemical equilibrium and kinetic problems, for multiple chemical species, gas concentration ranges and temperatures.

Several works have explored unconfined flames of methane / oxygen. Screenivasan[3] studied unconfined methane-oxygen laminar premixed flame numerically and experimentally. Transport equations for the steady, incompressible, laminar reactive flow in axisymmetric cylindrical coordinates were discretized by the Finite Volume Method through FLUENT 6.3[4] with

GRI-Mech 2.11[5] including 121 chemical reactions with 25 species. Predicted OH isopleths agreed with digital flame photographs, but the model over-predicted measured temperature near the axis and under-predicted at farther radial locations.

Bennett[6] studied axisymmetric laminar co-flow diffusion flames, which are fed by non-premixed parallel input gas streams of fuel and oxygen source. Computations using a solution-adaptive gridding method with both GRI-Mech 2.11 and GRI-Mech 3.0[7] chemical mechanisms predicted flame lengths, maximum centerline temperatures, radial temperatures and main species profiles that agreed well with measurements. Peak NO mass fraction predicted with GRI-Mech 3.0 were twice as large as from GRI-Mech 2.11. Increasing the oxygen source from air to pure oxygen produced a hotter, shorter flame, even if the fuel source was diluted from 65% to 20% methane in nitrogen. This is because the hotter flame attached to the burner due to significant reactant / burner preheating. Bhadraiah[8] used these measurements of laminar co-flow methane-oxygen diffusion flames[6] to compare a model with 43 combustion steps and 18 species, a model with four global reaction mechanisms, and an optically thin radiation sub-model, and had mixed findings.

For flow involving turbulent flames, Ogami[9] presented a numerical vortex method which incorporates chemical equilibrium, eddy-dissipation, and particle transport calculations to predict combustion of premixed methane and air. The predicted temperature and main reaction products matched with experiments. For confined combustion, Bidi[10] modeled turbulent premixed methane-air combustion in an axisymmetric cylindrical chamber using a chemical mechanism with 16 species and 31 reactions, and the k-ε turbulence model. Turbulent intensity was found to greatly affect flame behavior, temperature, and reaction product fractions. Silva[11] modeled turbulent non-premixed combustion of natural gas (methane) with air in a cylindrical chamber using the Eddy Breakup-Arrhenius model for chemical reactions, and a two-step combustion model. Compared with measurements, species mass fraction discrepancies were attributed to the preheated gases, which increased flame temperature rapidly and led to a faster consumption of reactants.

In addition to the above fundamental combustion studies, there is some research involving industrial torch heating, such as scarfing[12,13], and SEN preheating.[14-17] Zhou et al[12] developed a two-step model of heat transfer in a steel scarfing process. The model was validated with temperature measurements in the solid. It was found that the fraction of heat entering the steel from the scarfing reactions and adherent slag particles was relatively small. The heat lost by forced convection from the flame and the combustion product gases did not affect heat transfer much, relative to the scarfing reactions. Kim et al[13] studied the design of in-line edge scarfing nozzles by numerical analysis, using a 2D axisymmetric flow model, and species transport combustion model. The heat from the combustion gas to preheat oxygen was found to be important. Luo et al[14-17] modeled transient SEN temperature distributions in "combustion" and "fan type" preheating modes. Fan-type preheating was suggested to be better, in order to avoid bamboo joint shaped cracks at the neck of the nozzle.

Although there are many fundamental model studies of controlled methane / air or methane / oxygen combustion flames, very few models are found of torch heating in industrial applications using realistic chemical mechanisms. Thus, a 2D asymmetric model has been developed in the current work to simulate torch preheating that includes methane / oxygen / air combustion and transient heat transfer in the refractory. Measured flame temperature profiles, SEN wall temperature histories, flame shape, and SEN outer wall temperatures are used to validate the computational models, which are then applied to gain new insight into torch preheating practice.

EXPERIMENTAL MEASUREMENTS

An SEN preheating experiment was performed at Magnesita Refractories[1,2,18] which directed a turbulent flame produced from a premixed natural gas and oxygen stream downward into a SEN. Flow meters and pressure gauges were installed in the tubes which connected the natural gas tank and the oxygen tank to a pipe feeding the premixed gases into a burner tip. The mixed gas ejects from a W300 Rosebud burner tip supplied by ESAB[19]. After traveling a short distance to the top of the SEN, and entraining surrounding air as a partially free flame, most of the combustion occurs in the confined domain inside a typical two-port SEN. The SEN refractory is doloma-graphite (DG28XA-CT) with a 0.7mm-thick glaze layer coating on both the inner and outer surfaces of the SEN refractory to prevent oxidation. S-type thermocouples are utilized to measure the SEN wall and gas temperatures.

The experimental set-up including the flame shape during operation is pictured in Figure 1. The burner tip is positioned 97mm above the top of the SEN, which is referred to here as the "stand-off distance". At the burner tip, the cone-shaped flame is blue, which normally signifies high temperature and complete combustion. This flame is generated by contributions from all of the small orifices in the burner tip. As it moves downwards, the flame entrains air, cools, and extends about 300-400mm (12-16") down the bore of SEN, based on the experimental observations[2]. The gas temperature profile across the diameter of the SEN bore was measured by thermocouple No. 1, located 197mm below the top of the SEN. At the center of the port, gas temperature is measured by thermocouple No. 2 (not shown in Figure 1).

As shown in Figure 1, thermocouples No. 3 and No. 5 measure temperatures inside the SEN wall at an "upper level" (197mm below the SEN top), while thermocouples No. 4 and No. 6 measure at a "lower level" (341mm below the SEN top). Further geometry details are given in Figure 4 and Table 3. The temperature measurements are recorded every 10 seconds for ~115mins of this preheating experiment. Figure 2 shows an infra-red photo of the SEN outside wall, which was taken at ~50min after ignition, and is calibrated to show temperature contours.

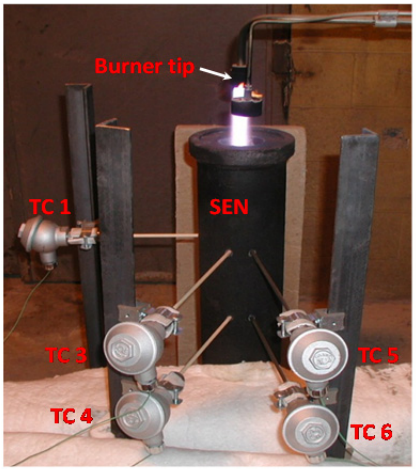

Figure 1. Preheating experiment setup[1]

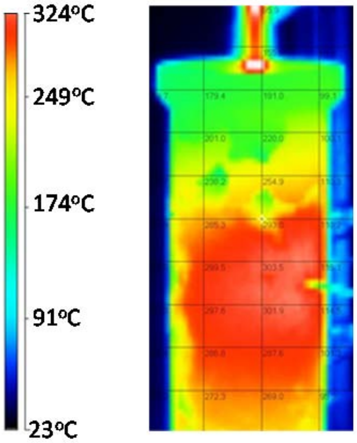

Figure 2. Infra-red photo of SEN outside wall[2]

Table 1 lists the flow rate and the pressure of methane and oxygen measured in the combustion experiment. SCFM means gas volumetric flow rate at standard conditions of 20 °C temperature and 101326 Pa pressure, and is transformed into actual conditions in the second column using the Ideal Gas Law (Equation 5). The calculated molar ratio of methane: oxygen is 5:4, which is a very fuel-rich mixture, which should produce yellow or yellowish flame color, due to the excess carbon. However, the flame color observed in the experiment is blue, which indicates a high temperature and complete combustion. This was explained by reported experimental uncertainty with the flow rate measurements compared with the pressure measurements. Based on these observations, the controversy was resolved by assuming that the methane flow rate was over-measured.

Therefore, complete combustion is assumed at the burner tip, which corresponds to a molar ratio of methane: oxygen as 1:2. Based on this ratio and the Ideal Gas Law, the best estimate of the methane flow rate is calculated in Equation 1. The corresponding total mass flow rate of the mixed gas exiting the burner tip is calculated in Equations 2-3.

$$\dot{V}_{CH4} = \frac{\dot{n}_{CH4} P_{O2} T_{CH4} \dot{V}_{O2}}{\dot{n}_{O2} P_{CH4} T_{O2}} = 8.78 \times 10^{-4} m^3/s \tag{1}$$

$$\dot{n}_{O2} = \frac{P_{O2} \times \dot{V}_{O2}}{R \times T_{O2}} = \frac{(310300 + 101325) * 6.97 * 10^{-4} m^3/s}{8.314 * 293.15} = 1.18 \times 10^{-1} mole/s \tag{2}$$

$$\dot{m}_{total} = \dot{m}_{CH4} + \dot{m}_{O2} = \dot{n}_{CH4} \times 16 + \dot{n}_{O2} \times 32 = 4.71 \times 10^{-3} kg/s \tag{3}$$

where $\dot{V}_{CH4}$ and $\dot{V}_{O2}$ is the volumetric flow rate of methane and oxygen respectively,
$\dot{n}_{CH4}$ and $\dot{n}_{O2}$ is the molar flow rate of methane and oxygen respectively,
P_{CH4} and P_{O2} is the absolute pressure of methane and oxygen respectively,
T_{CH4} and T_{O2} is the temperature of methane and oxygen respectively,
R is gas constant,
$\dot{m}_{total}$, $\dot{m}_{CH4}$ and $\dot{m}_{O2}$ is the mass flow rate of mixture, methane and oxygen respectively.

Table 1. Experiment data flow rate and pressure[2]

	Measured flow rate (SCFM)	Measured flow rate (m^3/s)	Gauge pressure (PSI)	Gauge pressure (kPa)
O_2	6	6.97×10^{-4}	45	310.30
CH_4	7.5	2.20×10^{-3}	9	62.06

COMBUSTION MODEL

A two-dimensional, (2D) axisymmetric model of non-premixed methane / oxygen / air combustion is developed for incompressible flow using FLUENT 13.0[20]. The first simulation is performed to validate this model with conditions matching the experimental measurements, which include the stand-off distance of 97mm (97mm Validation Case). Then, to demonstrate a model application, a second simulation was performed for the same conditions, but increasing the stand-off distance to 147mm (147mm Case).

Governing equations

The governing equations for the current 2D axisymmetric combustion model include the continuity equation (4), the momentum-conservation equation (6, 7), the turbulence equation (8-11), the energy conservation equation including chemical reactions (12-14), and the species transport equation (15).

Continuity equation:

$$\frac{1}{r}\frac{\partial}{\partial r}(r\rho v_r) + \frac{\partial}{\partial z}(\rho v_z) = 0 \tag{4}$$

The ideal gas law to relate gas density with temperature is:

$$\rho = \frac{PM}{RT} \tag{5}$$

where ρ is density (kg/m^3),
M is the molecular weight of the gas (kg/mol),
R is the universal gas constant (8.314 J/Kmol),
v_r is radial velocity (m/s),
v_z is axial velocity (m/s).

Axial (z) momentum conservation equation:

$$\frac{\partial}{\partial z}(\rho v_z v_z) + \frac{1}{r}\frac{\partial}{\partial r}(r\rho v_z v_r) = -\frac{\partial P}{\partial z} + \frac{1}{r}\frac{\partial}{\partial r}[\mu_{eff}\left(r\frac{\partial v_z}{\partial r} + \frac{\partial v_r}{\partial z}\right)] + \frac{1}{r}\frac{\partial}{\partial z}\left[r\mu_{eff}\left(2\frac{\partial v_z}{\partial z} - \frac{2}{3}(\nabla\cdot\vec{v})\right)\right] + \rho g \tag{6}$$

Radial (r) momentum conservation equation:

$$\frac{\partial}{\partial z}(\rho v_z v_r) + \frac{1}{r}\frac{\partial}{\partial r}(r\rho v_r v_r) = -\frac{\partial P}{\partial r} + \frac{1}{r}\frac{\partial}{\partial z}[\mu_{eff}\left(r\frac{\partial v_z}{\partial r} + \frac{\partial v_r}{\partial x}\right)] + \frac{1}{r}\frac{\partial}{\partial r}\left[r\mu_{eff}\left(2\frac{\partial v_r}{\partial r} - \frac{2}{3}(\nabla\cdot\vec{v})\right)\right] - 2\mu_{eff}\frac{\partial v_r}{\partial r^2} + \frac{2\mu_{eff}}{3r}(\nabla\cdot\vec{v}) \tag{7}$$

where P is static pressure (Pa),
μ_{eff} is effective dynamic viscosity (Ns/m^2).

Turbulent kinetic energy k:

$$\frac{\partial}{\partial z}(\rho v_z k) + \frac{1}{r}\frac{\partial}{\partial r}(r\rho k v_r) = \frac{\partial}{\partial z}\left[\left(\mu_{lam} + \frac{\mu_{tub}}{\sigma_k}\right)\frac{\partial k}{\partial z}\right] + \frac{1}{r}\frac{\partial}{\partial r}\left[r\left(\mu_{lam} + \frac{\mu_{tub}}{\sigma_k}\right)\frac{\partial k}{\partial r}\right] + G_k + G_b - \rho\varepsilon \tag{8}$$

Turbulent dissipation energy ε:

$$\frac{\partial}{\partial z}(\rho v_z \varepsilon) + \frac{1}{r}\frac{\partial}{\partial r}(r\rho\varepsilon v_r) = \frac{\partial}{\partial z}\left[\left(\mu_{lam} + \frac{\mu_{tub}}{\sigma_\varepsilon}\right)\frac{\partial \varepsilon}{\partial z}\right] + \frac{1}{r}\frac{\partial}{\partial r}\left[r\left(\mu_{lam} + \frac{\mu_{tub}}{\sigma_\varepsilon}\right)\frac{\partial \varepsilon}{\partial r}\right] + C_{1\varepsilon}\frac{\varepsilon}{k} - C_{2\varepsilon}\rho\frac{\varepsilon^2}{k} \tag{9}$$

$$\mu_{\mathrm{eff}} = \mu_{lam} + \mu_{tub}\rho C_\mu\frac{k^2}{\varepsilon} \tag{10}$$

$$\mu_{tub} = \rho C_\mu\frac{k^2}{\varepsilon} \tag{11}$$

where k is turbulence kinetic energy (kg m^2/s^2),
ε is turbulence dissipation energy (m^2/s^3),
μ_{lam} and μ_{tub} are laminar and turbulent viscosities (Ns/m^2),

G_k represents the generation of turbulence kinetic energy due to the mean velocity gradients (kg m^2/s^2),
G_b represents the generation of turbulence kinetic energy due to buoyancy (kg m^2/s^2),
σ_k, σ_ε, C_μ, $C_{1\varepsilon}$, $C_{2\varepsilon}$ are constants, 1, 1.3, 0.09, 1.44 and 1.87 respectively.

Energy conservation equation:

$$\frac{\partial}{\partial z}(\rho v_z h) + \frac{1}{r}\frac{\partial}{\partial r}(r\rho v_r h) = \frac{\partial}{\partial z}\left(D_h \frac{\partial h}{\partial z}\right) + \frac{1}{r}\frac{\partial}{\partial r}\left(r D_h \frac{\partial h}{\partial r}\right) + S_{rad} \tag{12}$$

$$\mathrm{h} = \sum_k Y_k h_k + \frac{P}{\rho} \tag{13}$$

$$h_k = \int_{T_{ref,k}}^{T} C_{p,k} dT + h_k^0(T_{ref,j}) \tag{14}$$

where D_h is thermal diffusivity (m^2/s),
S_{rad} is a radiation source term (W/m^3),
Y_k is the mass fraction of species k,
$h_k^0(T_{ref,j})$ is the formation enthalpy (J/kg) of species k at the reference temperature $T_{ref,k}$(K).

Species transport equations:

$$\frac{\partial}{\partial z}(\rho v_z Y_k) + \frac{1}{r}\frac{\partial}{\partial r}(r\rho v_r Y_k) = \frac{\partial}{\partial z}\left(\rho D_k \frac{\partial Y_k}{\partial z}\right) + \frac{1}{r}\frac{\partial}{\partial r}\left(r\rho D_k \frac{\partial Y_k}{\partial r}\right) + \dot{\omega}_k \tag{15}$$

where Y_k is the mass fraction of species k,
D_k is the mass diffusion coefficient of species k,
$\dot{\omega}_k$ is the rate of generation of species k (kg/m^{3}s).

Model domain, mesh and boundary conditions for 2 cases

In the experiment, the mixed gas ejects from multiple small orifices in the burner tip, where the pressure drops down to atmospheric pressure in a very short distance. To avoid the complications of locally-supersonic flow and mesh refinement problems, the model combines these two steps and simply assumes that the mixed gas exits the burner tip at atmospheric pressure, through a single, annular- shaped port with larger area of 4mm inner radius and 8mm outer radius, which is shown in Figure 3. The simulated area of the ports, 150 mm^2, is three times bigger than the actual, 48.7mm^2, to account for unmodeled gas expansion through the burner tip. Moreover, the two exit ports of this bifurcated SEN are simplified as a single ring-shaped axisymmetric port in the combustion model. The SEN port area is 11102 mm^2, and the assumed port length is 23mm with the 76mm outer radius.

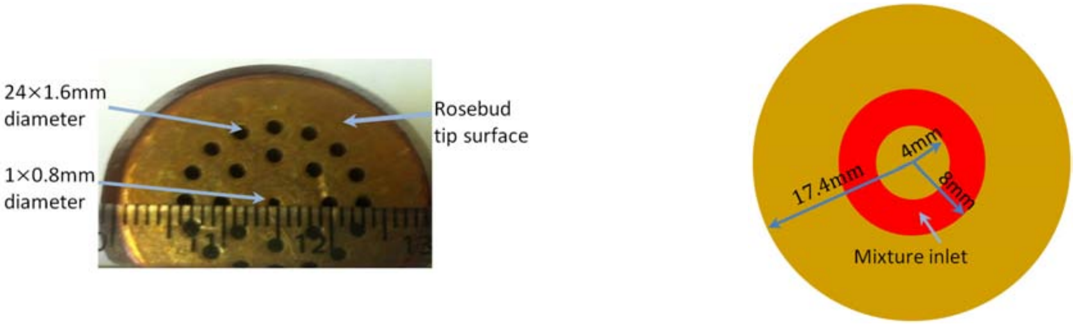

Figure 3. Burner tip geometry (a) photograph of W300 Rosebud tip (b) schematic of the burner used in the model

Figure 4 shows the model domain including SEN dimensions[21] for the 97mm Validation Case. The domain has 1100 mm axial length and 400 mm radius. The commercial meshing software GAMBIT 2.4.6[22] was employed to create the computational domain and to generate grids of quadrilateral cells. As shown in Figure 5, non-uniform grid spacing is used with finer grids near the burner tip, the SEN top, the port, and near the SEN wall and glaze layers. The minimum grid spacing is 0.25 mm in the glaze layers. The 97mm Validation Case contains 88843 cells. For the 147mm Case, the model domain is extended 50mm upward above the origin (z=0) in the axial direction, and contains the same number of cells.

Five kinds of boundary conditions are employed in the model.

(1) Burner tip inlet: The boundary condition at the burner tip is defined as a mass flow inlet. The mass flow rate is calculated based on oxygen / natural gas volumetric flow rates from the measurement. The operating absolute pressure at the burner tip is 101325 Pa, and the temperature is 3104.67^{o}C. The distance from the burner tip to where the combustion starts is very short, and can be neglected in the fluid flow model. The inlet gas compositions are 33.33% methane and 66.67% oxygen, according to Equation 1. Emissivity of the gas mixture at the burner tip inlet is taken as 0.035[24].

(2) Burner side wall and SEN internal walls: Standard no slip condition of $v_z = v_r = 0$, for fluid flow. Heat transfer at internal walls is by conduction, which involves coupling the boundaries of the flowing gas and solid glaze regions of the domain, and by radiation, using emissivity of 0.925[25].

(3) Domain top, bottom, and right side: All domain boundaries where air can enter or leave are defined as pressure outlets, where the oxygen mole fraction is 21.01% and the nitrogen mole fraction is 78.99%. Constant temperature 26.85^{o}C is specified at these boundaries for the atmospheric air, which entrains into or flow out of the domain. In the atmosphere, the air emissivity is very small, so emissivity 10^{-11} is chosen. The operating absolute pressure at the burner tip is 101325 Pa.

(4) Domain left side: This boundary represents the centerline axis of the SEN and the axisymmetric domain.

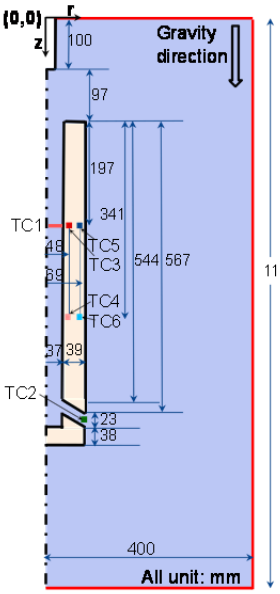

Figure 4. Combustion Model domain including SEN dimensions

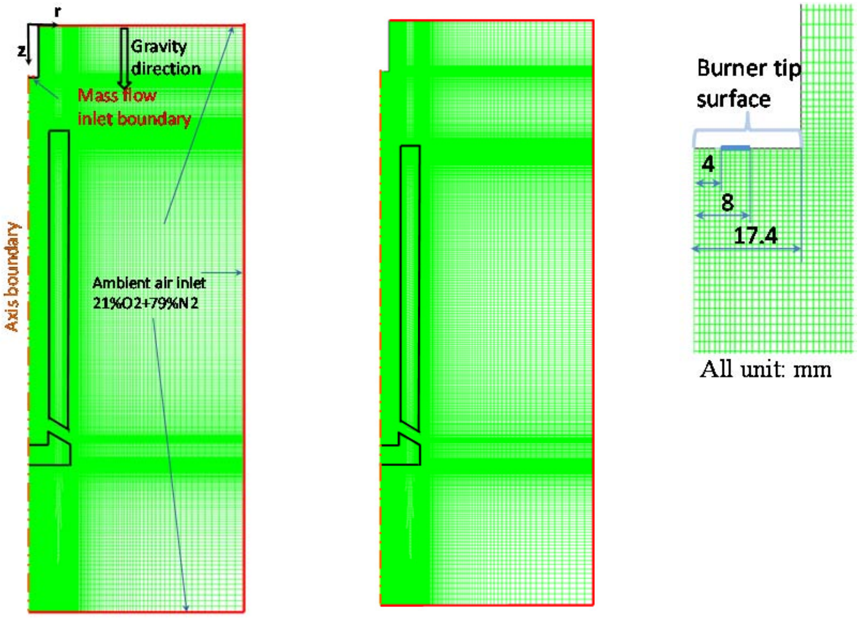

Figure 5. (a) 97mm Validation Case (b) 147mm Case (c) zoom-in inlet

Material properties

The temperature-dependent enthalpy of each gas species, mixture densities (PDF), specific heats of mixing, and reaction kinetics are provided via the thermodynamic database, GRI-Mech 3.0,[27] which contains 325 reactions and 53 species, and is called a "chemical mechanism" that is optimized to model natural gas combustion. The average gas viscosity 9.32×10^{-5} kg/ms and thermal conductivity 2.7006 W/mK are based on the weighted-average properties of the fuel, air and reacted gases from the literature[23]. In the P1 radiation model, the absorption coefficient is decided based on wsggm-domain-based method, assuming isotropic scattering with the scattering coefficient set to zero, and the refractive index is 1. The major species assumed to generate nonluminous radiation are the combustion products CO_2 and H_2O. For mixture gas emissivity at the burner tip (inlet) is calculated as 0.035[24]. The SEN wall material, density, conductivity, specific heat and glaze layer emissivity are listed in Table 2 based on measurements[18].

Table 2. SEN wall material properties[18]

Doloma Graphite	Temperature(°C)	Thermal conductivity (W/m K)	Specific Heat (J/kg K)	Density (kg/m^3)
	25	26.5	750	2330
	500	21.8	1228	
	1000	17.7	1360	
	1500	14.6	1481	
Glaze	25	0.90	821	2000
	200	1.20	1035	
	550	1.67	1281	
Emissivity[25]	1075	1.00	1611	
0.925	1425	0.40	1836	

Numerical details

Combustion is modeled in this work using a turbulent, non-premixed species model with a steady flamelet state relation and non-adiabatic energy treatment. The conservation equations for mass, momentum, species and energy for steady, incompressible, turbulent reactive flow in axisymmetric cylindrical coordinates (r, z) are discretized and solved with the Finite Volume Method using the commercial computational fluid dynamic software FLUENT-ANSYS 13.0[20]. A pressure based solver with operating pressure of 101325 Pa is applied. Gravitational acceleration in the axial direction (z) is included to model buoyancy effects. The standard k-ε turbulence model with enhanced wall treatment is used to describe the turbulent flow, using constants from Bilger[26] for turbulent flows with combustion. Steady laminar flamelet approach is applied to simplify the turbulent flame brush. The GRI-Mech 3.0 database is accessed from a database file, thermo.db, kept in the local working directory of FLUENT. P1 radiation model (with zero band) is applied on the flow, glaze inner and outer zones in the combustion model. Second order upwind schemes and SIMPLE algorithm for pressure-velocity coupling are used to discretize the governing equations. The convergence criterion for residual errors is 10^{-4} for the continuity, velocity and turbulence equations, and is 10^{-6} for the energy and P1 radiation equations. Table 3 lists important constants used in the model.

Table 3. Combustion Model Constants

Symbol / Definition	value
σ_k	1
σ_ε	1.3
C_μ	0.09
$C_{1\varepsilon}$	1.44
$C_{2\varepsilon}$	1.87
Energy Prandtl Number	0.7
Wall Prandtl Number	0.7
PDF Schmidt Number	0.7
burner tip inner radius	4 mm
burner tip outer radius	8 mm
97mm Case stand-off distance	97 mm
147mm Case stand-off distance	147 mm
SEN inner radius	37 mm
SEN outer radius	76 mm
axisymmetric port length	23 mm

AIR ENTRAINMENT AND ADIABATIC FLAME TEMPERATURE

A simple spreadsheet model developed by Singh[28] calculates adiabatic flame temperature. Given an input fuel, Oxygen Source Fraction, Air Entrainment, reactants pressure and temperature, the adiabatic flame temperature is calculated by a chemical equilibrium program, Gaseq[29], followed by a calculation of products properties, and convection coefficients at the SEN walls. This model has the ability to calculate SEN wall transient temperature, which is not shown in this work.

Oxygen Source Fraction is defined here as the molar ratio of oxygen input with the fuel relative to stoichiometric combustion reaction oxygen requirement of 100%. Air Entrainment is the molar ratio of extra outside air entrained relative to the amount of air that would be needed for stoichiometric combustion, neglecting the Oxygen Source. Equations to calculate Oxygen Source Fraction and Air Entrainment are given in Equations 16-17. In the preheating experiment, Oxygen Source Fraction can be calculated from the pressure, the temperature, and the volume flow rate of methane and oxygen respectively.

However, the amount of the entrained air can be hardly measured from the experiment. So the current combustion model is applied to simulate the preheating process, including an output of the air entrainment.

For a fuel with the general composition C_xH_y, the stoichiometric combustion reaction with a pure oxygen source is:

$$C_xH_y + (x + \frac{y}{4})O_2 = xCO_2 + \frac{y}{2}H_2O$$

$$\text{Oxygen Source Fraction} = \frac{\dot{n}_{O2}}{(x+y/4)\dot{n}_{fuel}} = \frac{\dot{m}_{O2}MW_{fuel}}{(x+y/4)\dot{m}_{fuel}MW_{O2}} = \frac{P_{O2}}{(x+y/4)P_{fuel}} \cdot \frac{\dot{V}_{O2}}{\dot{V}_{fuel}} \cdot \frac{T_{fuel}}{T_{O2}} \qquad (16)$$

For the same general fuel with composition C_xH_y, the stoichiometric combustion reaction with air is:

$$C_xH_y + \left(x + \frac{y}{4}\right)O_2 + 3.76\left(x + \frac{y}{4}\right)N_2 = xCO_2 + \frac{y}{2}H_2O + 3.76\left(x + \frac{y}{4}\right)N_2$$

$$\text{Air Entrainment} = \frac{\dot{n}_{air}}{4.76\left(x + \frac{y}{4}\right)\dot{n}_{fuel}} = \frac{\dot{m}_{air}MW_{fuel}}{4.76\left(x + \frac{y}{4}\right)\dot{m}_{fuel}MW_{air}} = \frac{\dot{n}_{N2}}{3.76\left(x + \frac{y}{4}\right)\dot{n}_{fuel}}$$

$$= \frac{\dot{m}_{N2}MW_{fuel}}{3.76\left(x+\frac{y}{4}\right)\dot{m}_{fuel}MW_{N2}} = \frac{\dot{n}_{+\_O2}}{\left(x+\frac{y}{4}\right)\dot{n}_{fuel}} = \frac{\dot{m}_{+\_O2}MW_{fuel}}{(x+y/4)\dot{m}_{fuel}MW_{O2}} \qquad (17)$$

where $\dot{n}$ is the molar rate (mole/s),
$\dot{n}_{O2}$ is the molar rate of oxygen provided by mixture at burner tip (mole/s),
$\dot{n}_{+\_O2}$ is the molar rate of oxygen provided by entrained air (mole/s),
P is the absolute pressure (Pa),
$\dot{V}$ is the volume flow rate(m^3/s),
T is the reactant temperature (K),
$\dot{m}$ is the mass flow rate (kg/s),
MW is the molecular weight (kg/mole).

Equation 17 indicates two methods to calculate the air entrainment from the results of the combustion model. Method 1 assumes that the extra mass flow rate entering the SEN at its top inlet surface is caused by the entrained air. Method 2 converts the nitrogen mass flow rate across the SEN top inlet into the corresponding entrained air. Table 4 lists the steps and results of both methods for the 97mm Validation Case, and they match well, considering numerical errors.

Table 4. Air Entrainment calculated from Combustion Model Results

Method 1		Method 2	
Mass flow rate at the burner tip	4.709 g/s		
Mass flow rate at the SEN top inlet	29.664 g/s	Methane mass flow at the burner tip	0.942 g/s
Entrained Air mass flow rate	24.955 g/s	Nitrogen mass flow rate at the SEN top inlet	19.148 g/s
Air Entrainment	153.7%	Air Entrainment	154.4%

The Singh[28] spread-sheet model predicts a flame temperature of 1334°C at equilibrium adiabatic conditions, for the 97mm Validation Case, based on reactant inlet conditions of 27 °C and 1 atm, 100% Oxygen Source Fraction and 154% Air Entrainment. This matches very closely with the average flame temperature at TC1-3-5 of 1343 °C from the comprehensive Combustion Model with FLUENT. Thus, the simple spread-sheet model can predict the flame temperature accurately without needing the sophisticated chemical reactions and thermal hydraulic models. The flame temperature and corresponding heating inside the SEN is controlled by the air entrainment.

For the 147mm Case, air entrainment of 135% and adiabatic flame temperature of 1456 °C are predicted. This result shows that increasing the stand-off distance gives a longer distance for the flame jet to spread before entering the SEN, which lessens the Venturi effect, and thus allows less air entrainment. With less air dilution, the gas temperature inside the SEN increases.

The equivalence ratio is commonly used to quantify the extent that a fuel-oxidizer mixture is fuel-rich, or fuel-lean, relative to the stoichiometric ratio. It is defined in Equation 18.

$$\emptyset = \frac{fuel\ to\ oxidizer\ ratio}{(fuel\ to\ oxidizer\ ratio)_{st}} = \frac{m_{fuel}/m_{ox}}{(m_{fuel}/m_{ox})_{st}} = \frac{n_{fuel}/n_{ox}}{(n_{fuel}/n_{ox})_{st}} = \frac{\dot{n}_{fuel}/\dot{n}_{ox}}{(\dot{n}_{fuel}/\dot{n}_{ox})_{st}} \qquad (18)$$

where “oxidizer” is the total oxygen mole flow rate composed of the oxygen at the mixture inlet and the oxygen from the entrained air.

$$\dot{n}_{O2} = \text{Oxygen source fraction} \times (x + y/4)\dot{n}_{fuel}$$

$$\dot{n}_{+\_O2} = \text{Air entrainment} \times (x + y/4)\dot{n}_{fuel}$$

In terms of the two parameters defined in Equations 16 and 17, the equivalence ratio is the inverted sum of the Oxygen Source Fraction and the Air Entrainment:

$$\emptyset = \frac{\dot{n}_{fuel}/\dot{n}_{ox}}{(\dot{n}_{fuel}/\dot{n}_{ox})_{st}} = \frac{\dot{n}_{fuel}/(\dot{n}_{O2}+\dot{n}_{+\_O2})}{\dot{n}_{fuel}/((x+y/4)\dot{n}_{fuel})} = \frac{1}{\text{Oxygen Source Fraction+Air Entrainment}} \qquad (19)$$

For the 97mm Validation Case, Oxygen Source Fraction is 100% and Air Entrainment is 154%, so the equivalence ratio is 0.397. For the 147mm Case, the equivalence ratio is 0.426.

MODEL VALIDATION

The combustion model was validated by comparing predictions of the 97mm Validation Case with the experimental measurements. First, Figure 6 compares measured and simulated temperature profiles across the inner bore of the SEN, along the path of thermocouple No. 1 measurements. Without considering one erroneous “measured” point that would have been inside the SEN wall, the simulated results match the trend of the measurements and consistently over-predict the gas temperatures by ~84 ^{o}C. However, gas temperature measurements should be corrected for the error caused by heat loss from the thermocouple junction due to radiation (to a colder environment) and the accompanying convection heat loss (due to the junction being colder). Conduction loss along the wire can be neglected for wires over 1mm long[30]. The following equation[30] is used to calibrate the measurement:

$$t_j = t_{T/C} + \sigma \varepsilon_{T/C} t_{T/C}^4 / h \qquad (20)$$

where t_j is the adjusted (corrected) thermocouple temperature,
$t_{T/C}$ is the measured thermocouple temperature,
σ is Stefan-Boltzmann constant,
$\varepsilon_{T/C}$ = 0.14 is probe emissivity (recommended for uncoated platinum Type B thermocouple),
h = 750 W/m^{2}K is convection coefficient for gas flowing over probe.

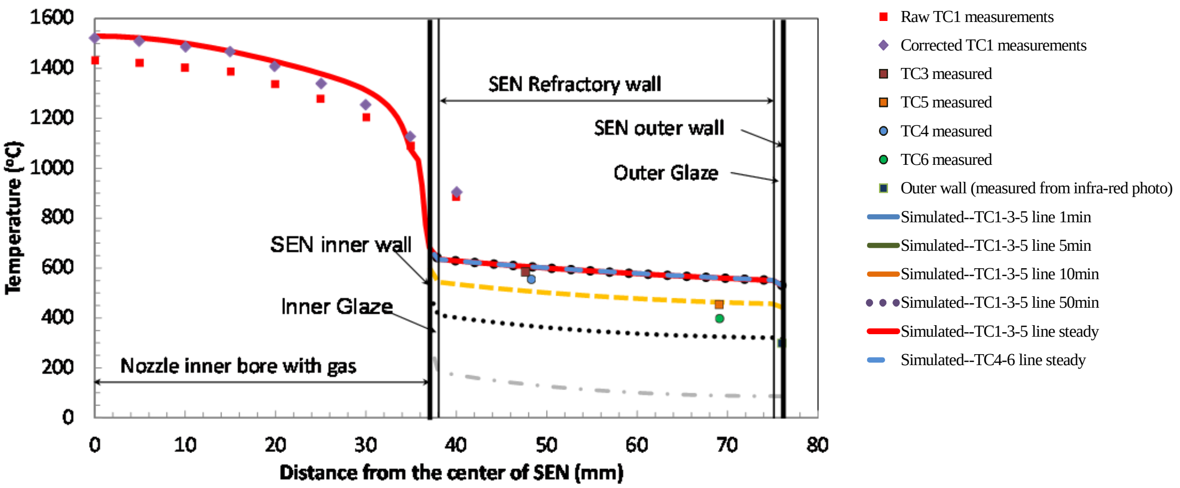

Figure 6. Temperature comparisons across the SEN

Figure 6 shows that the corrected gas temperature measurements match very well with simulations, with an average error of only ~14^{o}C (again without considering the point beyond the SEN inner wall).

Secondly, the combustion model predictions of temperature across the coated SEN wall are compared with the measurements of thermocouples embedded in the refractory in Figures 6 and 7. The model nozzle wall includes an “Inner Glaze” layer, the “Refractory wall” and an “Outer Glaze” layer. Due to the lower conductivity of the glaze, the temperature drops sharper at the inner and outer glaze layer. The transient model predicts that the SEN wall heat transfer almost reaches steady state after

~50minutes of combustion preheating. The model predictions of the temperature profile in Figure 6 show reasonable trends with the measurements in the SEN wall, but the temperatures at steady-state are higher, especially at the locations of thermocouples No. 5 and No. 6.

A sensitivity study[31] was conducted to investigate the importance of 20 different parameters affecting the temperature distribution in the nozzle wall. The effects of these parameters are listed in Table 5. From this study, the contact resistance caused by the contact-resistance gap between the tip of the thermocouple and the drilled hole in the SEN wall emerges as the most likely explanation of the discrepancy between the predicted and measured temperatures. Thus, the measurements were adjusted to account for this by:

$$T_{adjusted} = T_{measured} + \frac{(T_{measured} - T_{out_{air}})d_{gap}\sqrt{h\pi D k_{TC}}}{\sqrt{\pi}k_{air}D/2} \tag{21}$$

where $T_{adjusted}$ is the adjusted measured temperature,
$T_{measured}$ is the measured temperature,
T_{out_air} = 20℃ is the ambient temperature,
d_{gap} is the approximate calibrated air gap thickness,
k_{air} is thermal conductivity of the air gap between the thermocouple tip and the drilled hole,
h = 20 W/m^2 K is the heat transfer coefficient of the air along the TC,
k_{TC} = 200W/mK is the copper-constantan thermocouple thermal conductivity,
D = 4 mm is the thermocouple diameter.

The thermal conductivity of the gap is an important variable affecting the contact resistance which changes with temperature. From literature[20], the conductivity of air increases significantly with temperature and hydrogen content. Assuming that the gap contains air with 20% Hydrogen, the conductivity is given in Equation 22.[20] This equation was used in evaluating Equation 21 to adjust measured temperature.

$$k_{air} = 5 \times 10^{-5}T + 0.0451 \tag{22}$$

where T is the air gap temperature (^{o}C).

The air gap thickness for each thermocouple needed to calibrate the model to match the measured steady state temperature is, listed in Table 6. Gaps of only 1.5-15.0 microns can account for the lower measured temperatures. Figure 7 compares the measured, adjusted (adjusted measurement), and simulated refractory temperature histories. During transient heating (from start to ~50min), the simulation shows faster heat-up than the measurement and the adjusted temperature. One possible reason is that thermal expansion of the SEN wall during heating the refractory may cause relative movement of the refractory towards the thermocouple, which decreases the air gap thickness with increasing refractory temperature and time. Further adjustment of the measured temperatures using a growing gap would enable a perfect match with the simulation during transient heatup.

Thirdly, the predicted flame shape is compared with a close-up of the experimental flame photo in Figure 8. The 1800 ^{o}C temperature contour line lies on the flame rim in the photo, and shows that the predicted and observed flame shapes match well and exhibit continuous slight expansion along the length of the flame above the SEN.

Finally, Figure 9 compares the predicted SEN outer wall temperature contours with the infra-red photo in Figure 2. Both images show the same region of the SEN outer wall from the top of the SEN to 360mm below the top. The temperature contours show similar trends, where the lower region (~150mm to ~320mm below SEN top) is hotter, due to reattachment of the flame inside the nozzle. Quantitatively, the model overpredicts the temperature due to neglecting the changing thermal resistance of the gap, as previously discussed. Overall, the model predictions are very consistent with the measurements, so the model is considered to be validated.

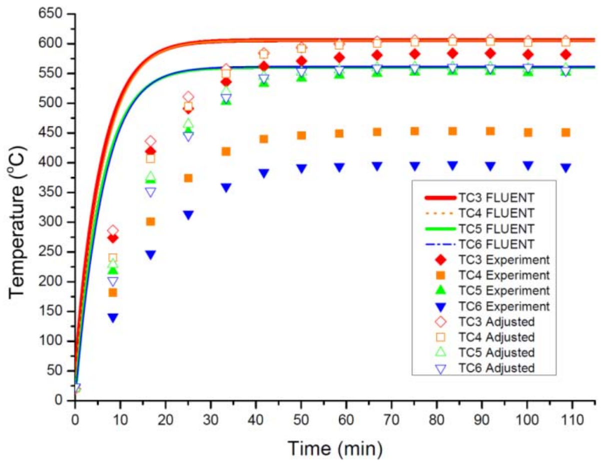

Figure 7. Transient wall temperature histories comparing model predictions, measurements, and adjusted measurements

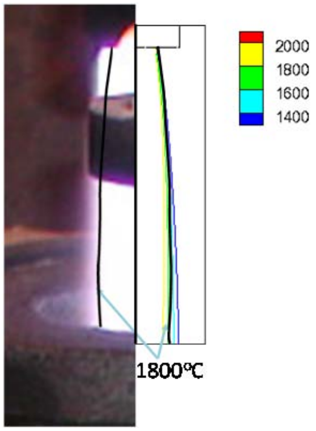

Figure 8 Flame shape comparisons of predicted temperature contours and the close-up photograph

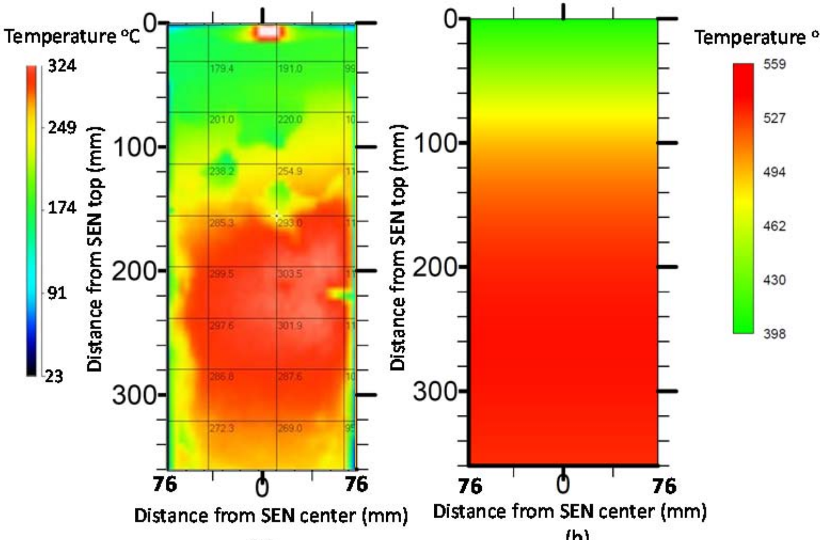

(a)

(b)

Figure 9. SEN outer wall temperature comparison (a) infra-red photo (b) 97mm Validation Case temperature contour

Table 5. Sensitivity analysis for steady state[31]

Independent variable					Standard(618°C)	Measured(458°C)
					Diff Temp(°C)	Diff Temp(°C)
No.	Xi	Standard	Estimated uncertainty	New condition		
1	T_in (°C)	1200	-500	700	-283	-123
2	T_out_air(°C)	20	-15	5	-4	+156
3	h_in_convect(W/m^{2}K)	70	-50	20	-154	+5
4	h_out_convect(W/m^{2}K)	20	-15	5	+115	+275
5	Gas emissivity	0.1	-0.099	0.001	-111	+49
6	Gas emissivity	0.1	+0.4	0.5	+152	+311
7	glaze and refractory emissivity	0.5	-0.4	0.1	+120	+280
8	glaze and refractory emissivity	0.5	+0.4	0.9	-92	+68
9	k_refractory (W/mK)	20	+20	40	+12	+171
10	k_glaze (W/mK)	1	+1	2	+5	+165
11	k_glaze (W/mK)	1	+19	20	+10	+170
12	R_in_glaze(mm)	36.6	-2	34.6	-63	+97

13	R_in_glaze(mm)	36.6	+0.7	37.3	+24	+184
14	R_in_refractory(mm)	37.3	+2	39.3	-45	+114
15	R_out_refractory(mm)	77.3	-2	75.3	+23	+183
16	R_out_glaze(mm)	78	-0.7	77.3	-6	154
17	R_measure point(mm)	67.2	+2	69.2	-3	157
18	R_measure point(mm)	67.2	-2	65.2	3	163
19	T_in_wall(℃)	700	+3	703	+1	+161
20	T_out_wall(℃)	550	+22	572	-10	+150
21	d_{gap}(mm)	0.5	+0.5	1	+1194	+1354
22	k_{air}(W/mK)	1	+9	10	+60	+219
23	h(W/m^2 K)	20	-15	5	+300	+458
24	k_{TC}(W/mK)	200	-190	10	+134	+293
25	$T_{out\ air}$(℃)	20	+200	220	+397	+556

where h_in_convect is the convection heat transfer coefficient of the inside nozzle,
h_in_convect is the convection heat transfer coefficient of the inside nozzle,
h_out_convect is the convection heat transfer coefficient of the outside nozzle,
h_in_radi is the radiation heat transfer coefficient of the inside nozzle gas,
h_out_radi is the radiation heat transfer coefficient of the outside nozzle gas,
h_in_total is the sum of convection and radiation heat transfer coefficient of the inside nozzle,
h_out_total is the sum of convection and radiation heat transfer coefficient of the outside nozzle,
T_in is the gas product temperature of the inside nozzle,
T_out_air is the air temperature outside the nozzle,
T_in_wall is the temperature of the inside wall of the nozzle,
T_out_wall is the temperature of the outside wall of the nozzle,
k_refractory is the thermal conductivity of the refractory,
k_glaze is the thermal conductivity of the glaze,
R_in_glaze is the radius of the glaze at the inside nozzle,
R_in_refractory is the radius of the inside of the refractory,
R_out_refractory is the radius of the outside of the refractory,
R_out_glaze is the radius of the glaze of the outside nozzle,
R_measure point is the location of the thermocouple.

Table 6. Air gap thickness at thermocouple tip

	TC3	TC4	TC5	TC6
Combustion Model (^oC)	607	604	561	561
Measurement (^oC)	584	554	453	397
Gap thickness (μm)	1.52	3.53	8.77	14.98

RESULTS AND DISCUSSION

Further results from the validated model are presented: species concentration, fluid flow, gas temperature and SEN temperature. The distance that the nozzle is positioned above the SEN has an important effect on the air entrainment, combustion, and subsequent temperature evolution in the nozzle refractory. This was investigated in a brief parametric study consisting of two simulations: the 97mm Validation case, compared with a new case where the nozzle tip was moved further above the SEN, to 147mm.

Species concentration

Mole-fraction contours of the main species are shown in Figure 10 for the 97mm Validation Case. Oxygen mole fraction (a) is 67% at the burner tip inlet boundary, defined by the stoichiometric gas / fuel mixture. As combustion progresses, oxygen is consumed and is almost totally depleted in the flame product gases. However, entrained air drawn into the SEN top via the Venturi effect diffuses and causes oxygen to increase to 13%~20% further down the nozzle. Nitrogen fraction (b) also indicates the effect of the entrained air. Although there is no nitrogen at the burner tip, the air drawn into the SEN increases Nitrogen to over 50%, which distributes evenly by lower in the SEN. Methane fraction (c) drops sharply as the fuel burns. Carbon monoxide fraction (d) increases in the flame region during combustion to a maximum of 15% in the flame just above the SEN., This combustion product decreases with distance down the SEN both because it is diluted by air and because it further oxidizes, being consumed as a fuel to form CO_2 as temperature drops. Carbon dioxide fraction (d) increases to almost 6% and then decreases, initially in a similar manner as CO. Towards the SEN bottom, however, CO_2 increases again, as CO transforms into CO_2 with lowering temperature. Water fraction (e) increases during combustion to reach a maximum of 19% above the SEN top. It decreases due to diffusion and air dilution but later increases slightly towards the SEN bottom as other non-equilibrium products such as H, OH and H_2 finally near completion of their oxidation reactions.

Fluid flow results

Stand-off distance of the burner tip changes the gas flow distribution in the domain, especially the entrainment of air. Figures 11 and 12 show velocity vectors for the 97mm Validation Case and 147mm Case, respectively. For both cases, the flow exiting from the burner tip is the fastest, due to the rapid expansion that accompanies combustion. The fast jet flow into the top of the SEN entrains air from the surroundings. As turbulent flow diffuses the jet momentum, the velocity profile across the nozzle becomes more uniform with distance down the SEN. Direction arrows (a) in the whole domain show directions of entrained air, especially at the top, bottom and right side boundaries. As shown in Figure 11 (a), the air enters into the domain vertically at the top boundary, and changes direction towards SEN inner gradually due to Venturi effect. However, in 147mm Case, flame spread more before entering the SEN with farther stand-off distance, and thus less air entrainment. In Figure 15, 147mm Case shows higher temperature in both gas and solid regions. Due to the stronger buoyance effect caused by higher temperature near to the SEN wall, more air rises near the SEN outer wall and exits the top boundary as shown in Figure 12 (a). Velocity scales in SEN inner zoom-in vectors (b) in Figure 11 and 12 show the entrained air velocity is much smaller compared with fuel stream velocity near the burner, which decreases to ~60m/s evenly by lower in the SEN. In both figures, zoom-in vectors near the SEN top (c) gives a closer view at the entrained air direction near the SEN top, where the velocity increases at the rim of flame rim.

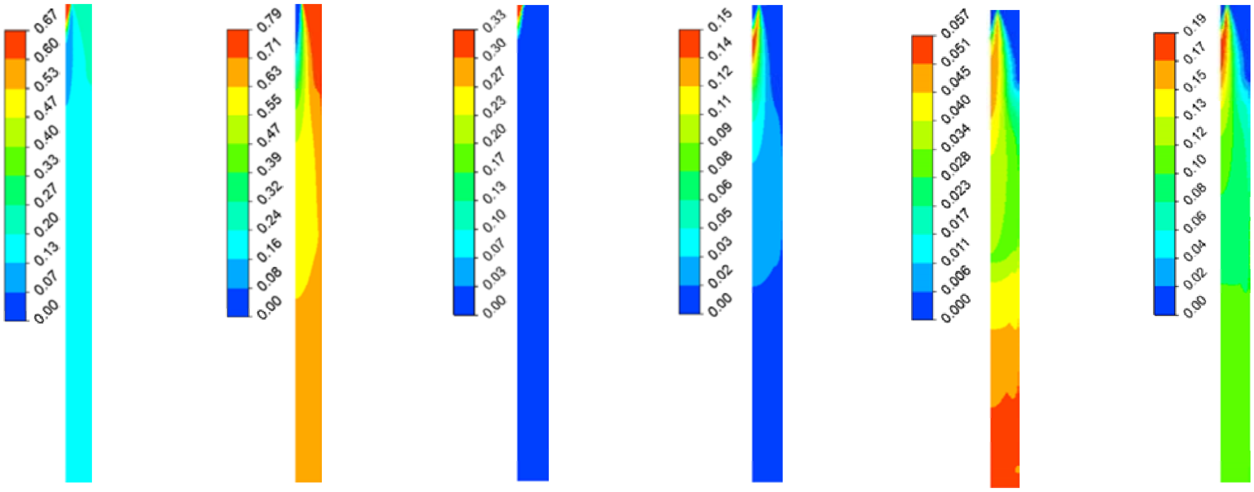

O_2 Mole Fraction N_2 Mole Fraction CH_4 Mole Fraction CO Mole Fraction CO_2 Mole Fraction H_2O Mole Fraction

(a) (b) (c) (d) (e) (f)

Figure 10. Mole fraction contours of main species (97mm Validation Case)

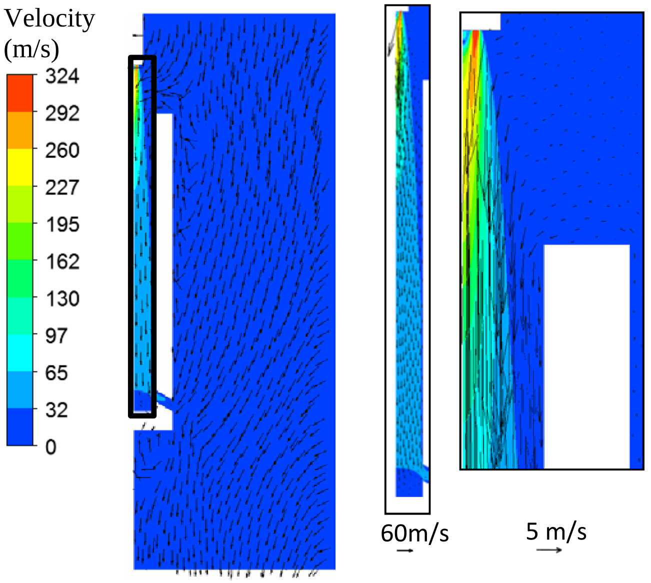

(a) (b) (c)

Figure 11. Flow pattern (97mm Validation Case)
(a) direction arrows in the whole domain
(b) velocity vectors inside SEN
(c) zoom-in vectors near SEN top

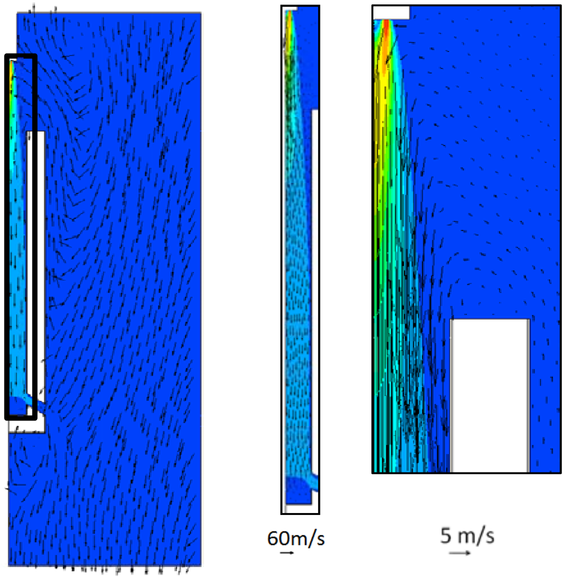

(a) (b) (c)

Figure 12 Flow pattern (147mm Case)
(a) direction arrows in the whole domain
(b) velocity vectors inside SEN
(c) zoom-in vectors near SEN top

Gas temperature

Figures 13 and 14 show gas temperature profiles across the SEN inner bore at different distances below the SEN top for the 97mm Validation Case and 147mm Case, respectively. For both cases, near the top of the SEN, the temperature drop across the SEN from the center to the inner wall is the largest. Cold air is drawn into the SEN along the inner walls, which generally causes lower temperature near the inner wall. As the gases mix, temperature profiles are flattened with distance down the SEN. Towards the lower part of the SEN, some heat is released due to delayed combustion of CO into CO_2, especially near the walls where there is slightly more oxygen, due to the air entrained down the inside walls. Thus, the temperature at 341mm below SEN top at TC4-6 is slightly higher at the walls.

Compared with the 97mm Validation Case, the 147mm Case shows slightly lower temperature entering the center of the SEN top because the flame is colder with a farther stand-off distance. Inside the SEN, however, the 147mm Case shows higher and more uniform gas temperatures at both axial locations of TC1-3-5 and TC 4-6, owing to less air entrainment and heat lost to that air, as discussed in detail in the next section.

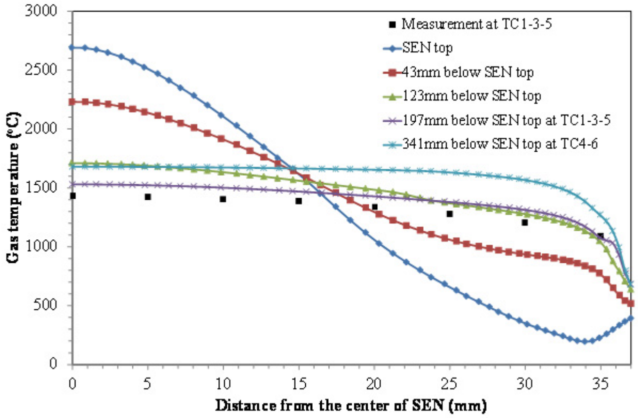

Figure 13. Gas temperature profiles across SEN inner bore at different distances below SEN top (97mm Validation Case)

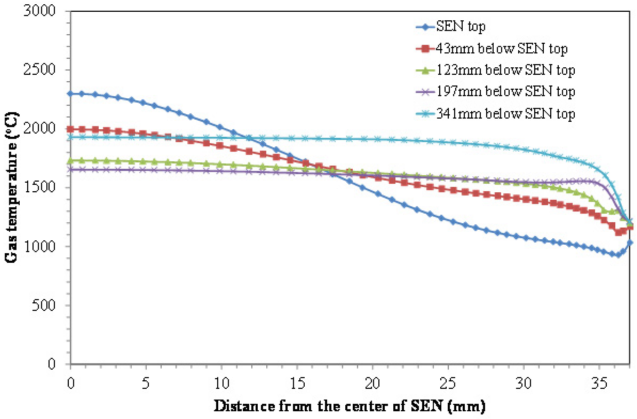

Figure 14. Temperature profiles across the SEN inner bore at different distances below SEN top (147mm Case)

SEN temperature

Temperature contours in the whole domain are shown in Figure 15 for the two cases with 97mm and 147mm stand-off distances. Temperature is ~1400 ^{o}C at the inner of nozzle at both cases. The upper part of the SEN wall temperature is low, until the flame jet spreads enough to touch the SEN inner wall. After the flame diffuses and impinges the inner wall, the lower part of the SEN wall is heated greatly. For the 97mm Validation Case, temperature contours (a), show the hottest temperature is 3229 ^{o}C at 26mm below the burner tip, and gas temperature at the port center drops to 927 ^{o}C. For the 147mm Case (b) temperature is higher everywhere. This is because the flame jet ejected from the burner tip has a longer distance to spread before entering the SEN, which reduces the air entrainment from 154% to 135%. This lessens the heat lost to heating that air. Owing to its strong effect on air entrainment, the flame shape entering the SEN is very important to temperature inside the SEN and thus to preheating efficiency.

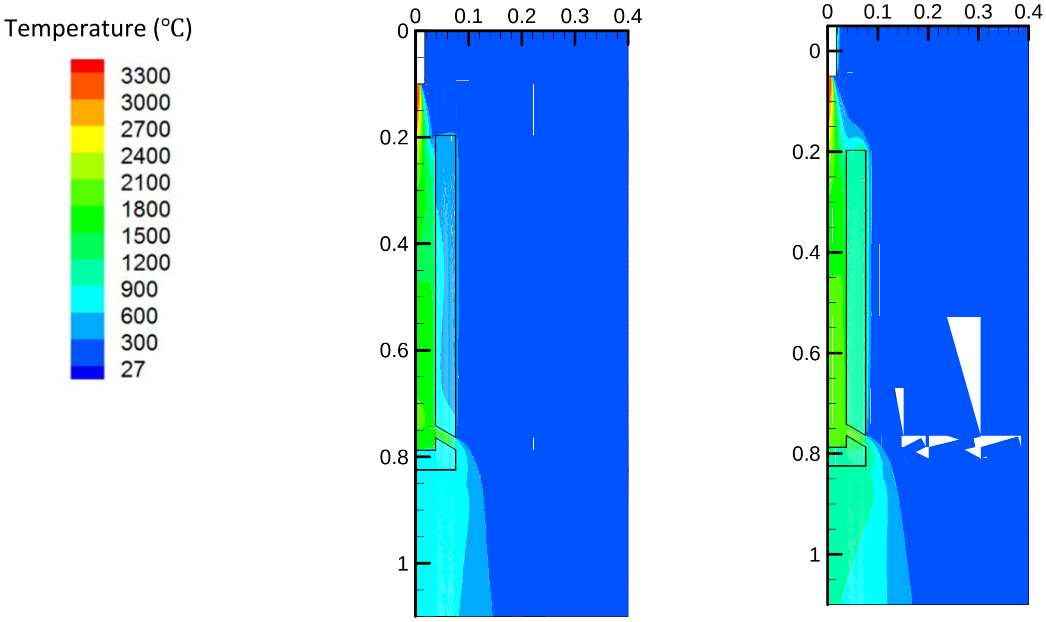

Figure 15. Steady-state temperature contours (a) 97mm Validation Case (b) 147mm Case

CONCLUSIONS

In this work, a 2D axisymmetric model of nozzle preheating is developed using FLUENT with GRI-Mech 3.0 to include 325 non-equilibrium chemical reactions with 53 species to simulate methane combustion. The finite-volume computational model simulates steady-state fluid flow, heat transfer, and combustion in the gas and transient heat conduction in the SEN walls. The model predictions were validated with experimental measurements of a preheating experiment, including the corrected temperature profile across the flame, temperature histories measured inside the SEN wall, the flame shape, and the SEN outer wall temperature distribution. A simple spread-sheet model of the adiabatic flame temperature is shown to accurately predict the gas temperature inside the SEN, based on knowing the air entrainment. The validated nozzle preheating model was then applied to investigate the effect of stand-off distance. Moving the burner further away from the SEN top leads to higher SEN temperature and shorter preheating time, which is caused by less air entrainment due to longer distance for the flame to spread before it enters confined by the SEN. To optimize preheating, a proper stand-off distance, stoichiometric fuel composition, and insulation layers are recommended.

ACKNOWLEDGEMENTS

The authors are grateful to R. Nunnington and other personnel at Magnesita Refractories for providing the measurement data, and for support from the Continuous Casting Consortium at the University of Illinois.

REFERENCES

1. R. Nunnington, Magnesita Refractories, private communication, Jun, Aug 2012
2. Magnesita Refractories, PB10 SEN Temperature Data for CCC Heat Flow Model, Report, York, March 31st, 2010
3. R. Screenivasan, An investigation of flame zones and burning velocities of laminar unconfined methane-oxygen premixed, *Combustion Theory and Modeling*, Vol. 16, No. 2, 2012, 199-219
4. ANSYS® Academic Research, Release 6.3, Software, ANSYS, Inc.

5. C.T. Bowman, R.K Hanson, D.F. Davidson, W.C. Gardiner Jr, V. Lissianski, G.P. Smith, D.M. Golden, M. Frenklach and M. Goldenberg, GRI-Mech Home Page, http://www.me.berkeley.edu/gri mech/flames
6. B. Bennett, Computational and experimental study of oxygen-enhanced axisymmetric laminar methane flames, *Combustion Theory and Modeling*, Vol. 12, No. 3, 2008, 497-527
7. G.P. Smith, D.M. Golden, M. Frenklach, N.W. Moriarty, B. Eiteneer, M. Golderberg, C.T. Bowman, R.K. Hanson, S. Song,W.C. Gardiner, Jr., V.V. Lissianski and Z. Qin, GRI version 3.0. 1999. Available online at: http://www.me.berkeley.edu/gri mech (accessed 23 March 2007).
8. K. Bhadraiah, Numerical Simulation of laminar co-flow methane-oxygen diffusion flames: effect of chemical kinetic mechanisms, *Combustion Theory and Modeling*, Vol. 15, No. 1, 2011, 23-46
9. Y. Ogami, Simulation of combustion by vortex method, *Computers & Fluids,* Vol. 39, 2010, 592-603
10. M. Bidi, A Numerical Investigation of Turbulent Premixed Methane-Air Combustion in a Cylindrical Chamber, *Combust. Sci. and Tech.*, Vol. 179, 2007, 1841-1865
11. C. Silva, Numerical Simulation of the Combustion of Methane and Air in a Cylindrical Chamber, Vol. 5, 2006, June, 13-21
12. X. Zhou and B. G. Thomas, Modeling Steel Slab Heat Transfer During Scarfing Processing, Report to POSCO, Jul 2010
13. S. Kim and B. G. Thomas, "Design of In-line Edge Scarfing Nozzle Using Numerical Analysis", Final Report, POSCO-UIUC Joint Research, Jan 2008
14. H. Luo and X. Zhang, Study of preheating temperature field of submerged nozzle in burning method, Refractories, Mar 2003
15. H. Luo and X. Zhang, Temperature Field of Submerged Nozzle under Different Prehenating Regime, Steelmaking, Jan 2005
16. Y. Yang and H. Luo, Numerical Simulation of Preheating Temperature Field of Immersed Nozzle, Foundry Tech., Sep 2006
17. S. Liu, Temperature field of submerged entry nozzle during preheating, Steelmaking, Feb 2009
18. Magnesita Refractories, AG_DG thermal data_Feb 2011, Material properties measurement, 2011
19. ESAB welding torch W-300 Rosebud, available online at: http://esab.ca/esab/dbReplacement/pdf/17563_1143820097.pdf
20. ANSYS® Academic Research, Release 13.0, Software, ANSYS, Inc.
21. Magnesita Refractories, HT Project Dimensions update Aug24_ 2010, blueprint and measurement, 2010
22. Gambit 2.4.6 software
23. Charles E. Heat Transfer in Industrial combustion, p469
24. B. Leckner, Spectral and total emissivity of water vapor and carbon dioxide, Comb. Flame, 19, 33-48, 1972
25. R. Nunnington, Radiation measurement, Magnesita Refractories, 2011
26. R.W. Bilger, Prog. Energy Combustion. Sci., 1, 87-109, 1976
27. Gregory P. Smith, David M. Golden, Michael Frenklach, Nigel W. Moriarty, Boris Eiteneer, Mikhail Goldenberg, C. Thomas Bowman, Ronald K. Hanson, Soonho Song, William C. Gardiner, Jr., Vitali V. Lissianski, and Zhiwei Qin Avaliable at http://www.me.berkeley.edu/gri_mech/
28. V. Singh, Flame temperature VBA model, Excel software, University of Illinois at Urbana-Champaign, 2010
29. Gaseq, Chemical equilibrium program, available at http://www.gaseq.co.uk/
30. D. Bradley and K. J. Matthews, Measurements of high gas temperatures with fine wire thermocouples, J. Mech. Eng. Sci. 10(4), 299-305, 1968
31. Y. Li, Sensitivity Analysis Report of Preheat Process in SEN Nozzle at Steady State, University of Illinois, Aug 2011